Journal of the Serbian Society for Computational Mechanics / Vol. 19 / No. 1, 2025 / pp 451-462 / review paper
(10.24874/jsscm.2025.19.01.29)

COMPUTATIONAL MODELING OF DRUG TRANSPORT AND PERFUSION WITHIN COMPLEX BIOLOGICAL SYSTEMS AND GROWING TUMORS

Vladimir Simic[1] [0000-0001-7842-8902], **Miljan Milosevic**[1,4] [0000-0003-3789-2404], **Bogdan Milicevic**[1] [0000-0002-0315-8263] , **E.J. Koay**[3] [0000-0001-7675-3461], **Xuewu Liu**[3] [0000-0002-8702-0295], **Antonio Martino**[3,5] [0009-0008-0719-4668], **Rossana Terracciano**[3,5] [0000-0001-5026-0589], **Carly S. Filgueira**[3,5] [0000-0002-3246-303X], **Milos Kojic**[1,2,3,5*] [0000-0003-2199-5847]

[1] Institute for Information Technologies, University of Kragujevac, Kragujevac, Serbia
e-mail: **vsimic@kg.ac.rs**, **bogdan.milicevic@uni.kg.ac.rs**
[2] Serbian Academy of Sciences and Arts, Belgrade, Serbia
e-mail: **mkojic42@gmail.com**
[3] Houston Methodist Research Institute, The Department of Nanomedicine, Houston, USA
e-mail: **EKoay@mdanderson.org**, **xliu@houstonmethodist.org**, **ross.terracciano@gmail.com**
[4] Belgrade Metropolitan University, Belgrade, Serbia
e-mail: **miljan.m@kg.ac.rs**
[5] Department of Materials Science and Engineering, University of Houston, Houston, USA
e-mail: **amartino@houstonmethodist.org**, **csfilgueira@houstonmethodist.org**

**corresponding author*

Abstract

Mass transport is a fundamental process in living organisms, responsible for the delivery of oxygen, nutrients, and drugs from blood vessels to tissues, as well as the removal of waste products back to the vascular and lymphatic systems. This exchange occurs across various biological barriers, including blood vessel walls and cellular membranes, and involves complex mechanical and biochemical interactions. Traditional experimental and clinical methods have provided valuable insights into mass transport, but due to the complexity and heterogeneity of biological systems, computational models are essential for deeper understanding. Here, we give a brief review of a smeared modeling concept, termed the Kojic Transport Model (KTM), for gradient-driven physical fields within composite media such as biological tissue. The basic idea of the KTM is the formulation of the composite smeared finite element (CSFE). This element is composed of volumetric domains with different physical fields that are coupled by connectivity elements at each FE node representing biological barriers. The domains include 1D fields represented by 3D continuum form by formulation of the consistent transport tensors The KTM has been implemented in our finite element package PAK and demonstrated to be accurate and robust in modeling. We have selected models of mass transport (diffusion and perfusion) in the liver, pancreas, and tumor which grows over time.

Keywords: mass transport, perfusion, Kojic Transport Model (KTM), liver, pancreas

1. Introduction

Mass exchange is a vital process in all living organisms, occurring at multiple levels—from blood vessels down to the interior of cells and their organelles. Along this route, molecules such as oxygen, metabolic byproducts, and drugs move through different environments, including blood, extracellular fluid, the cell interior, and organelles, while crossing biological barriers like vessel walls and cellular or organelle membranes. Although considerable progress has been made, many aspects of mass transport remain poorly understood; particularly the biophysical mechanisms that govern drug delivery. Current research in this area relies largely on laboratory studies and experimental approaches.

Convection and diffusion are the fundamental processes regarding transport of molecules or particles (e.g. nanoparticles used in drug delivery) from the cardiovascular system to tissue and interior (cytosol and organelles). The interdisciplinary scientific field where the mass transport is studied, related to drug delivery by applying nanoparticles as the drug carriers to tumor sites, is named oncophysics (Ferrari, 2010; Koay and Ferrari, 2014). Mass transport in tumors is strongly influenced by perfusion, affecting oxygenation, nutrient delivery, waste removal, and drug efficacy. Studies on blood flow in tumor vasculature have shown that it is influenced by factors such as geometric resistance (Sevick and Jain, 1989) (which reflects network irregularities), viscous resistance, and the mechanical properties of red blood cells (RBCs). The dysfunctional tumor vasculature disrupts convective transport and diffusion, leading to hypoxia, drug resistance, and metabolic shifts. Targeting these transport limitations is a key strategy in improving cancer treatment outcomes.

For modeling particulate transport in complex organs and tumors, we employ standard laws of extracellular transport: Darcy's law for convection and Fick's law for diffusion (Kojic, 2008). Due to the computational challenges of resolving physical fields such as pressure or concentration within whole organs or tissues, we developed a smeared mass transport methodology for capillaries and tissue (Kojic et al., 2017a; 2017b; Milosevic et al., 2018; Kojic et al., 2018a; Kojic, 2018b; 2019). This approach, termed the Kojic Transport Model (KTM), generalizes to any gradient-driven field and has demonstrated advantages over conventional models (Kojic et al., 2022). Here, we present the KTM framework and illustrate its application to three cases: liver, pancreas, and tumor growth.

The primary computational tools used in this research include the Finite Element Analysis (FEA) software PAK (Kojic et al., 2019) (Program za Analizu Konstrukcija - an abbreviation in Serbian for Program for Structural Analysis), along with CADFiS (Milosevic, 2020) - a 3D graphical interface software for designing the computational models and visualization of results.

2. Methodology

Here, we first summarize the basic laws and equations in differential form which are further used in our KTM formulation.

2.1 Flow through porous media

For incompressible fluid flow through a porous rigid medium, the governing equation is given by Darcy's law:

$$v_i = -k_{Dij}\frac{\partial p}{\partial x_j},\ \textit{sum on } j:\ j=1,2,3 \tag{1}$$

where v_i is the Darcy velocity (as fluid flux per unit area of the continuum) in direction x_i, p is fluid pressure and k_{Dij} is the Darcy tensor. The mass balance equation is

$$k_{Dij}\frac{\partial^2 p}{\partial x_i \partial x_j}+q_V=0 \tag{2}$$

where q_V is a source term.

2.2 Diffusion

The constitutive law for diffusion is known as Fick's law,

$$Q_i=-D_{ij}\frac{\partial c}{\partial x_j} \tag{3}$$

and the mass balance equation is

$$-\frac{\partial c}{\partial t}-v_i\frac{\partial c}{\partial x_i}+\frac{\partial}{\partial x_i}\left(D_{ij}\frac{\partial c}{\partial x_j}\right)+q_V=0,\quad sum\ on\ i,j:\ i,j=1,2,3 \tag{4}$$

Here, c is concentration, Q_i flux and D_{ij} is the diffusion tensor. The generality is kept under the assumption that the diffusion tensor can be a function of concentration, i.e. it can be $D_{ij}=D_{ij}(c)$.

2.3 1D-conditions

Further, we consider mass transport the expressions for the 1D conditions. For fluid flow, these conditions represent the relations for flow within pipes (Smith et al., 2002). In the case of a rigid pipe, the governing equation can be expressed as

$$k_{pipe}\frac{\partial^2 p}{\partial \bar{x}^2}=0 \tag{5}$$

where $\bar{x}$ is the pipe direction and k_{pipe} is the pipe resistance coefficient which can be derived from the so-called Hagen-Poiseuille law. Additional terms are present in this equation for the case of deformable pipe (Kojic et al., 2014), but are not used here.

In the case of diffusion, the 1D condition follows from equation (4),

$$-\frac{\partial c}{\partial t}-v\frac{\partial c}{\partial \bar{x}}+\frac{\partial}{\partial \bar{x}}\left(D\frac{\partial c}{\partial \bar{x}}\right)+q_v=0 \tag{6}$$

where v is the fluid velocity and D is the diffusion coefficient.

2.4 Finite element formulation

The governing equations above can be converted into finite element (FE) balance equations for a single element using the standard Galerkin weighting method (Kojic et al., 2008, Kojic et al., 2022). The incremental-iterative balance formulation for a time step Δt and iteration i can be derived in the form

$$\left(\frac{1}{\Delta t}\mathbf{M}+\mathbf{K}^v+\mathbf{K}\right)^{(i-1)}\Delta\mathbf{\Phi}^{(i)}=\mathbf{Q}^{ext}+\mathbf{Q}^V-\frac{1}{\Delta t}\mathbf{M}^{(i-1)}\left(\mathbf{\Phi}^{(i-1)}-\mathbf{\Phi}^t\right)-\left(\mathbf{K}+\mathbf{K}^v\right)^{(i-1)}\mathbf{\Phi}^{(i-1)} \tag{7}$$

where

$$
\begin{aligned}
M_{IJ} &= \int_V c_m N_I N_J dV \\
K^v_{IJ} &= \int_V v_i N_I N_{J,i} dV, \quad \text{sum on } i: \; i = 1,2,3 \\
K_{IJ} &= \int_V D_{km} N_{I,k} N_{J,m} dV, \quad \text{sum on } k,m: \; k,m = 1,2,3 \\
Q^V_I &= \int_V N_I q_v dV
\end{aligned}
\tag{8}
$$

where $\mathbf{\Phi}$ stands for pressure or concentration as nodal variables; N_I are the interpolation functions, V is element volume; c_m is the rate coefficient (=0 for fluid flow, and =1 for diffusion); D_{km} is diffusion or the Darcy tensor; for the case of Darcy's flow or no convection, the convection matrix $\mathbf{K}^v$ is equal to zero

In the case of 1D problems, the equations have the same form as the above, with one index k and no summation; and the element volume is $V=AL$, where A is the cross-sectional area and L is the element length. The implicit integration scheme over time is used, i.e. all variables are evaluated at the end of the time step and the current equilibrium iteration. This integration scheme is unconditionally stable and provides the best accuracy (Kojic and Bathe, 2005).

3. Smeared modeling concept (KTM) and Composite Smeared Finite Element (CSFE) formulation

To introduce the smeared methodology, we first consider a detailed model of a composite medium (Fig. 1a), comprising continuum domains (extracellular space, cells, and organelles) and a network of fiber-like 1D domains (capillaries, lymphatic vessels, and neural fibers). Continuum domains exhibit a hierarchical structure, as cells may contain organelles, and each domain is discretized with a finite element (FE) mesh: continuum elements for continuum regions and 1D elements aligned with the axes of fiber-like structures. Connectivity elements (A–F in Fig. 1a) couple the domains at common boundary nodes. These elements are assigned transport coefficients based on membrane or wall properties, cross-sectional areas $\boldsymbol{A_m}$ corresponding to nodal surfaces, and lengths $\boldsymbol{h_m}$ representing membrane or wall thickness.

The detailed model description highlights the significant effort required for its generation. In the case of complex media like tissue, creating such a model would be impractical or even impossible. This challenge becomes even greater when using continuum finite elements (FEs) for membranes instead of connectivity elements. To address this, we have introduced a composite smeared model by formulating a continuum composite finite element (CSFE). This approach integrates all constituents (both continuum and 1D elements) in a way that preserves the true physical fields of the detailed model but represents them in an averaged (smeared) manner, ensuring sufficient accuracy. Figure 1b illustrates the smeared model for the same detailed setup as in Figure 1a, but with only continuum elements.

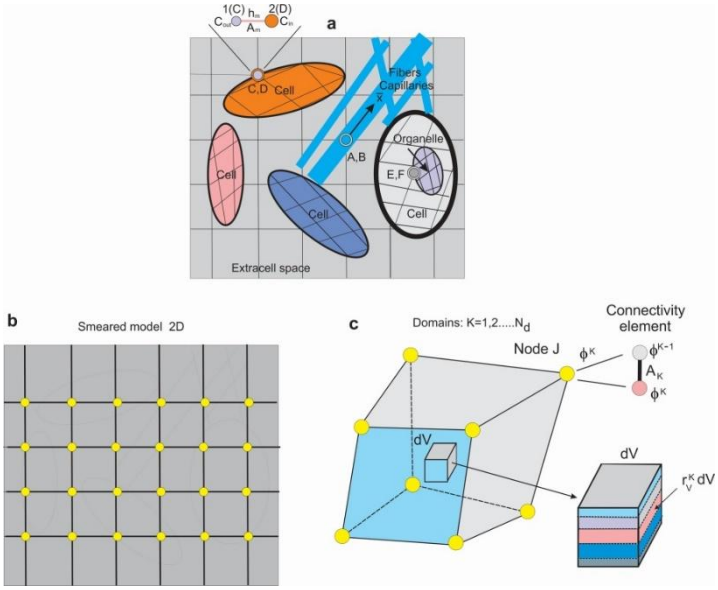

Fig. 1. Schematic representation of the detailed and smeared models: (a) A detailed model of tissue as a composite medium, with continuum subdomains and capillaries/fibers in a 2D view, including continuum, 1D, and connectivity elements; (b) Smeared finite element (FE) representation of the detailed model; (c) Composite smeared finite element (CSFE) with subdomains and a connectivity element at FE node *J*. (According to Kojic et al., 2018a).

The formulation of the CSFE element (Figure 1c) involves several conceptual steps, which are given in our previous publications (Kojic et al., 2017a; Kojic et al., 2017b; Milosevic et al., 2018; Kojic et al., 2018a; Kojic, 2018b, Kojic et al., 2019). Briefly, we first transform the 1D field equations into a 3D form by introducing transport tensor as

$$D_{ij} = \frac{1}{A_{tot}} \sum_K D_K A_K l_{Ki} l_{Kj} \tag{9}$$

where D_K, A_K and l_{Ki} are transport coefficient, cross-sectional area and directional cosine for 1D segment, respectively; A_{tot} is the total area of all 1D segments in the vicinity of the considered spatial point. Then, as shown in Fig. 1, we represent the continuum by the 3D CSFEs. The CSFE is divided into domains occupying volumetric fractions r_{vK} each with its physical field. The balance equations of the form (7), with the matrices for a domain K:

$$\begin{aligned} M_{IJ}^K &= \int_{V^K} r_V^K c_m^K N_I N_J dV, \quad K_{IJ}^{vK} = \int_{V^K} r_V^K v_i N_I N_{J,i} dV \\ K_{IJ}^K &= \int_{V^K} r_V^K D_{km} N_{I,k} N_{J,m} dV, \quad Q_I^{VK} = \int_{V^K} r_V^K N_I q_V dV \end{aligned} \tag{10}$$

Connectivity elements are introduced at each FE node to couple the corresponding domains. The balance equations for each 2-node element can be written in the form (7) with the element matrices

$$M_{IJ}^J = r_{AV}^J r_V^J V^J \int_{h_J} c_w^J N_I N_J dh, \quad K_{11}^J = -K_{22}^J = r_{AV}^J r_V^J D_w^J V^J \tag{11}$$

where r_{AV}^J, r_V^J are area-to-volume ratio, volumetric fraction; V^J is the volume belonging to the node J; c_w^J and D_w^J are the rate constant and wall transport coefficient. The connectivity elements represent the biological barriers (in this equation of the thickness h_J), such as the capillary wall or cell membrane.

4. Numerical examples

We present three numerical examples to highlight the key features of our smeared modeling methodology. These examples demonstrate the applicability of the KTM to large biological systems. The models are implemented in our finite element (FE) code, PAK, with a dedicated CAD interface developed at the R&D Center for Bioengineering BIOIRC.

4.5 Liver model with tumors

The liver and vascular geometry were reconstructed at the R&D Center BIOIRC using micro-CT scans of a mouse liver, with imaging performed by the Preclinical Imaging Core at the Houston Methodist Research Institute. The resulting finite element (FE) model (Fig. 2) consists of 7,736 1D pipe elements representing larger vessels, 39,832 3D composite smeared elements, and 726 connectivity elements linking the major vessels to the continuum nodes of the smeared FE mesh, i.e., the capillary domain. Two tumors are incorporated into the model, represented by 316 elements. In total, the model comprises 54,590 nodes. Full data for this example are reported in (Kojic et al. 2019).

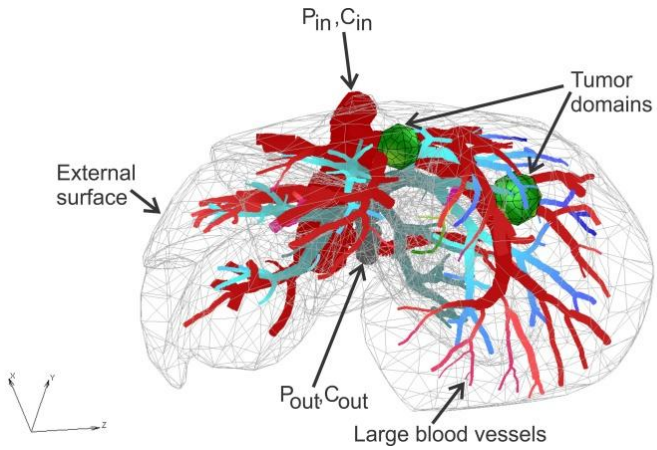

Fig. 2. Liver model geometry with two tumors and pressure distribution field within large vessels (inlet and outlet pressure and concentration branches marked). (According to (Kojic et al., 2019)).

Our goal was to show the difference in concentration between the two tumors, assuming the 10 times smaller diffusion coefficient within tumor 2 than in tumor 1. Figure 3 shows the pressure field for two views of the model: for the outer surface of 3D smeared elements, cross-section, and a dotted representation of large vessels and continuum. Tumor surfaces are indicated by dashed lines. There is a clear reduction in pressures - from large vessels to capillaries and further to tissue.

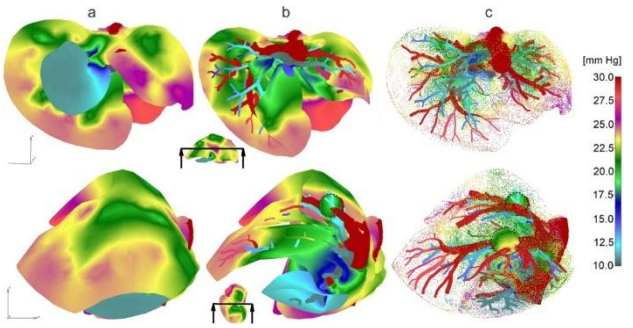

Fig. 3. Liver model geometry with two tumors and pressure distribution field within large vessels (inlet and outlet pressure and concentration branches marked). (According to (Kojic et al., 2019)).

The concentration field within large vessels, liver tissue, and tumors is shown in Fig. 4a for three time points. It is noticeable that concentrations have the largest values in blood vessels (practically the same due to convection and large diffusion coefficient in fluid), following a decrease going to capillaries and tissue. Also, the concentration within tumor 2 is smaller compared to tumor 1 due to reduced diffusion coefficients. Evolution of the mean concentration within capillaries (capillary domain) and tissue of the liver, and tumors 1 and 2, is shown in Fig. 4b. The model gives insight into the transport of particles or molecules within the entire organ. In the first period, when the entering mass is increasing (entering concentration is increasing), concentration within capillaries and tissue is increasing. The maximum concentration within capillaries has a delay with respect to the maximum of entering c(t); and the maximums in tissue and tumors have further delays. Also, transport continues from capillaries to tissue as long as the concentration within capillaries is larger than in tissue. It is evident that concentration in tumor 1 is higher than in tumor 2 due to the larger diffusion and partitioning coefficients

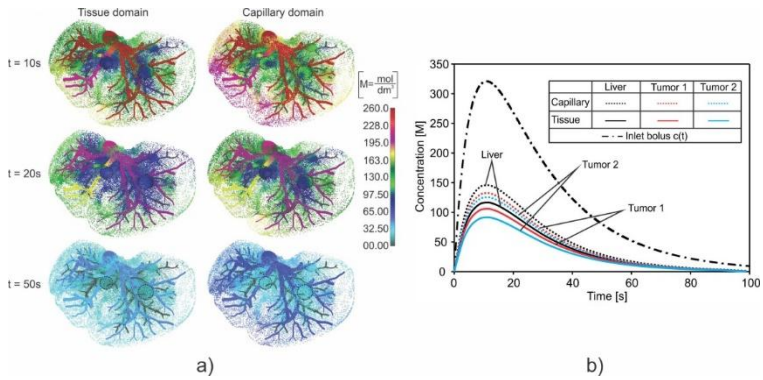

Fig. 4. a) Concentration field in the liver with tumors (marked with dashed lines), dotted results in tissue domain and with full mesh in tumors, for times t =10, 20, and 50s. b) Concentration evolution in the liver. The inlet concentration c(t) at the large vessel has a bolus character and generates bolus-type profiles of the mean concentrations in capillaries and tissue of the liver and within tumors – reduced with respect to c(t). The lowest concentration is in tumor 2 with the smallest diffusion and partitioning coefficient. (According to (Kojic et al., 2019))

4.6 Pancreas model

This model was chosen due to its distinct geometry, blood vessel size, and capillary volumetric fraction compared to other tissues, and the goal of enhancing the understanding of drug delivery for pancreatic cancer. The material properties and entering concentration bolus are assumed to be the same as in the liver model. The model is generated in the R&D Center BIOIRC according to the CT imaging from the MD Anderson Cancer Institute, Houston, under an approved Institutional Review Board protocol (PA14-0646). The model's geometry is shown in Fig. 5a. As in the previous example, we have here the 1D pipe finite elements (1602 elements) representing larger vessels, 3D composite smeared elements (104,884 elements), and connectivity elements (312 elements) that link large vessels to the capillary domain of the smeared finite elements. The total number of nodes is 127,783.

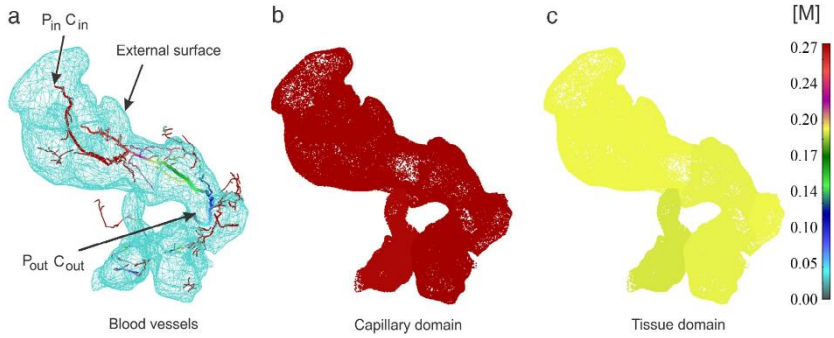

Fig. 5. Pancreas model. Concentration distribution at t=40s. (a) Geometry and concentration in large vessels; (b) Capillary domain concentration; (c) Tissue domain concentration (According to (Kojic et al., 2017a)).

Figure 6 displays the concentration fields at the end of the first time step (t=40s) within large vessels, as well as the capillary and tissue domains. Due to the lower capillary volumetric fraction, the concentration difference between capillaries and tissue is more pronounced compared to the liver model (Figure 4a).

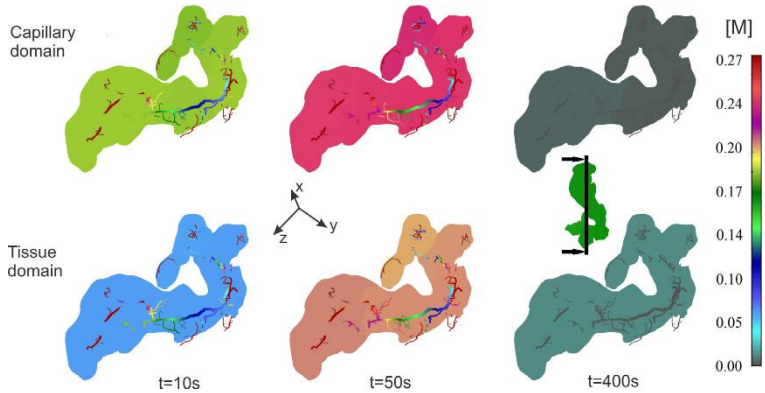

Fig. 6. Pancreas model. Concentration field within vertical plane for capillary and tissue domains, for three time steps. (According to (Kojic et al., 2017a))

4.7 2D model of perfusion within solid murine lung cancer growing tumor

The computational methodology employed for finite element (FE) model generation is briefly summarized below. Comprehensive descriptions of the 2D tumor imaging protocol, heatmap construction, and derivation of material parameters are available in (Martino et al., 2024). The FE model is reconstructed from the representative imaging data presented in (Martino et al., 2024) (Figures 3i, 3v, 3ix, and 3xiii), wherein the tumor domain is discretized using a structured 9×9 mesh. A uniform intravascular pressure of 10 mmHg is prescribed within the capillary network to incorporate the combined effects of hydrostatic and oncotic pressures, as well as contributions from arteriolar and venular segments. This pressure serves as a physiological driving force for interstitial fluid exchange between the capillaries and the extracellular matrix within the tumor microenvironment. Furthermore, a Dirichlet boundary condition of zero pressure is imposed along the outer contour of the computational domain, in accordance with (**https://courses.lumenlearning.com/suny-ap2/chapter/capillary-exchange**), under the assumption of equilibrium between fluid perfusion and reabsorption at the capillary–interstitium interface.

Based on the referenced figures in the previous paragraph, tumor contours were extracted from six individual tumors at 15% of total volumetric growth to compute an average geometry, which served as the initial configuration for the simulations. Additional contour data were obtained from subsequent imaging corresponding to 25%, 60%, and 80% of total tumor growth, enabling the determination of mean geometrical configurations at these specific growth stages. During the finite element simulations, boundary contours—encompassing both shape and size—were linearly interpolated between these experimental time points to model the temporal evolution of tumor geometry based on the averaged configurations.

Next, we applied the experimentally averaged vasculature, capillary diameter, and permeability to our model (Figures 3ii-iv, vi-viii, x-xii, and xiv-xvi in (Martino et al., 2024)). In this process, to assign all the data, equation solutions are interpolated using the inverse of the distance between two nodes as a weighting factor in accordance with the position of the final element node within the averaged heatmaps. Within each timepoint of the finite element computation, remeshing was performed, allowing for finite elements not to be fixed in space by their size or shape, since geometry evolves during calculations. Evaluation of the capillary volumetric fraction, r_{Vcap}, is performed as follows (described here for the parameters at 15% of the tumor growth). The averaged vasculature is first assumed to be equivalent to the capillary internal surface (A_{cap}) divided by the total surface of the cell grid (A_{tot}) to yield a percentage $A_{cap}= 100A_{cap}/ A_{tot}$, and then expressed in terms of the capillary diameter (d) and capillary length (L), as

$$A_{cap}^{\%} = \frac{100A_{cap}}{A_{tot}} = \frac{100d\pi L}{A_{tot}} \tag{12}$$

to provide an experimental derivation of A_{tot}. Since capillary volume can be expressed as $V_{cap}= d^2\pi L/4$, we can then obtain capillary volumetric fraction r_{Vcap} at a point of the surface as

$$r_{Vcap} = \frac{V_{cap}}{A_{tot}h_z} = \frac{d\pi L}{400h_z}A_{cap}^{\%} \tag{13}$$

where h_z=1 μm is the model thickness in the direction normal to the plane. Evaluation of the volumetric fraction of the extracellular space (r_{ex}), is performed as follows. The average permeability is assumed to be equivalent to the area covered by the cells (A_{cell}) divided by the total surface of the cell grid (A_{tot}) to yield cell volumetric fraction (r_{Vcell}), where $r_{Vcell}=A_{cell}/A_{tot}$. We then express the volumetric fraction of the extracellular space (r_{ex}) as

$$r_{ex} = 1 - r_{Vcap} - r_{Vcell} \tag{14}$$

Finally, the wall hydraulic coefficient h_{cap}^{J} is obtained from the filtration coefficient (K_f) in (**https://courses.lumenlearning.com/suny-ap2/chapter/capillary-exchange**) reduced to unit surface and expressed as 1.57×10^{-3} μm/(s Pa). We include perfusion anisotropy within the tumor since the volumetric fractions of the capillaries and extracellular space vary over the model domain in accordance with our experimental records.

Figure 7 illustrates the spatial and temporal evolution of interstitial pressure within the tumor at four selected time points: 7, 10, 13, and 16 days post-implantation. Pressure fields at each time point were obtained via interpolation from the preceding time point's finite element mesh to the current configuration, thereby ensuring the continuity of data and numerical stability required for successive simulations. In Figure 7A, pressure distributions are visualized as contour maps generated using our in-house CAD environment integrated with finite element analysis tools. Figure 7B presents a three-dimensional profile of pressure values along two orthogonal cross-sections (x- and y-axes) intersecting the tumor center. Notably, maximum pressure values exhibit minimal variation across the investigated time span, with a modest increase observed at day 16, which correlates with a reduction in extracellular volume fraction. Elevated pressure values originate near the tumor core and propagate toward the periphery.

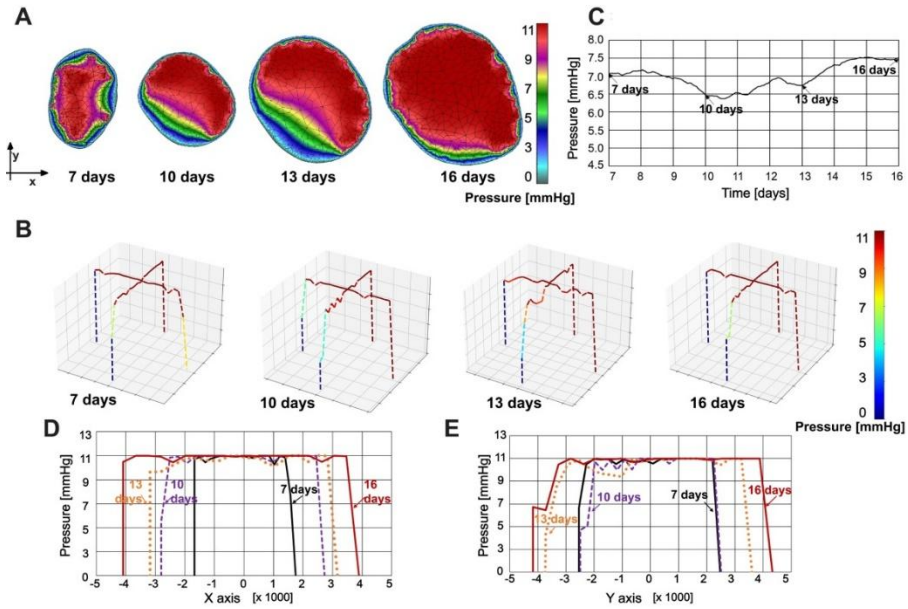

Fig. 7. (A) Pressure field at 7, 10, 13, and 16 days. (B) Pressure field in a 3D representation at 7, 10, 13, and 16 days. (C) Mean pressure vs time. (D) Pressure distribution along x-axis. (E) Pressure distribution along y-axis. (According to (Martino et al., 2024))

Figure 7C provides a temporal profile of the mean intratumoral pressure, offering insights into pressure progression during tumor growth. Spatial pressure distributions are further detailed in Figures 7D and 7E. Due to the requirements of the computational model—including defined geometries and boundary conditions—data presented in Figures 7C and 7D are confined to the interval between day 7 (corresponding to 15% tumor growth) and day 16 (80% tumor growth). While linear interpolation could theoretically be extended to time points outside this interval, such extrapolation would necessitate assumptions regarding geometry and growth dynamics

that are not empirically validated, thereby limiting its reliability. In both spatial directions (x and y), pressure is maximal at the tumor center and decreases radially toward the boundary, ultimately approaching zero. As evidenced in Figures 7C–E, pressure exhibits a nonuniform temporal evolution, with the configuration at day 16 showing a noticeable increase compared to that at day 7.

Figure 7C provides a temporal profile of the mean intratumoral pressure, offering insights into pressure progression during tumor growth. Spatial pressure distributions are further detailed in Figures 7D and 7E. Due to the requirements of the computational model—including defined geometries and boundary conditions—data presented in Figures 7C and 7D are confined to the interval between day 7 (corresponding to 15% tumor growth) and day 16 (80% tumor growth). While linear interpolation could theoretically be extended to time points outside this interval, such extrapolation would necessitate assumptions regarding geometry and growth dynamics that are not empirically validated, thereby limiting its reliability. In both spatial directions (x and y), pressure is maximal at the tumor center and decreases radially toward the boundary, ultimately approaching zero. As evidenced in Figures 7C–E, pressure exhibits a nonuniform temporal evolution, with the configuration at day 16 showing a noticeable increase compared to that at day 7.

5. A summary and concluding remarks

This paper presents the smeared modeling approach, termed Kojic Transport Model (KTM), as an effective tool for simulating mass transport and drug delivery within complex biological systems, including specific conditions within tumors. The methodology is developed in a way that relies on measurable material parameters. Here, the KTM is validated through numerical examples of whole-organs simulations, such as liver and pancreas, demonstrating both accuracy and applicability to real physiological conditions. Also, we examined tumor-specific biophysical properties throughout the dynamic process of tumor growth and utilized experimental data to develop a mathematical model capable of predicting the spatial and temporal evolution of intratumoral fluid pressure and velocity in three dimensions. Continued refinement and validation of this model will enhance our understanding of the tumor microenvironment, enabling improved prediction of therapeutic efficacy across diverse cancer subtypes.

The KTM as a general concept has the potential to support the rational design of drug delivery systems, optimize dosing strategies, and the development of more personalized and effective treatment regimens. While primarily applied to biomedical investigations, its potential extends to other complex transport systems, including non-biological environments like soils.

Acknowledgements: This research was funded by the National Institutes of Health, U01CA244107. Research is also supported by the Ministry of Education, Science and Technological Development of the Republic of Serbia, contract number [451-03-68/2022-14/ 200378 (Institute of Information Technologies, University of Kragujevac)], the Serbian Academy of Sciences and Arts, grant number F-134. We also appreciate the support from the City of Kragujevac, Serbia.

References

Ferrari M. Frontiers in cancer nanomedicine: directing mass transport through biological barriers. Trends Biotechnol. 2010;28(4):181-8

Koay EJ, Ferrari M. Transport oncophysics in silico, in vitro, and in vivo. Preface. Phys Biol. 2014;11(6):060201.

Kojic M, Milosevic M, Simic V, Milicevic B, Geroski V, Nizzero S, et al. Smeared multiscale finite element models for mass transport and electrophysiology coupled to muscle mechanics. Front Bioeng Biotechnol. 2019 Dec 10;7:381. doi: 10.3389/fbioe.2019.00381. PMID: 31921800; PMCID: PMC6914730.

Kojic M, Bathe KJ. Inelastic analysis of solids and structures. Berlin, Heidelberg, New York: Springer; 2005.

Kojic M, Filipovic N, Stojanovic B, Kojic N. Computer modeling in bioengineering: theoretical background, examples and software. Chichester (UK): John Wiley & Sons; 2008..

Kojic M, Milosevic M, Kojic N, Koay EJ, Fleming JB, Ferrari M, et al. Extension of the composite smeared finite element (CSFE) to include lymphatic system in modeling mass transport in capillary systems and biological tissue. J Serb Soc Comput Mech. 2017;11:108-20.

Kojic M, Milosevic M, Simic V, Ferrari M. A 1D pipe finite element with rigid and deformable walls. J Serb Soc Comput Mech. 2014;8:38-53.

Kojic M, Milosevic M, Simic V, Koay EJ, Fleming JB, Nizzero S, et al. A composite smeared finite element for mass transport in capillary systems and biological tissue. Comput Methods Appl Mech Eng. 2017a;324:413-37.

Kojic M, Milosevic M, Simic V, Koay EJ, Kojic N, Ziemys A, et al. Multiscale smeared finite element model for mass transport in biological tissue: from blood vessels to cells and cellular organelles. Comput Biol Med. 2018a;99:7-23.

Kojic M, Milosevic M, Simic V, Ziemys A, Filipovic N, Ferrari M. Smeared multiscale finite element model for electrophysiology and ionic transport in biological tissue. Comput Biol Med. 2019;108:288-304.

Kojic M. Smeared concept as a general methodology in finite element modeling of physical fields and mechanical problems in composite media. J Serb Soc Comput Mech. 2018b;12:1-16.

Kojic M, Milosevic M, Ziemys A. Computational models in biomedical engineering: finite element models based on smeared physical fields: theory, solutions, and software. Amsterdam: Elsevier; 2022.

Kojić M, Slavković R, Živković M, Grujović N, Filipović N. PAK-FE software for structural analysis, field problems, multiphysics and biomechanics. Kragujevac: Faculty of Mechanical Engineering; 1998/2010.

Martino A, Terracciano R, Milićević B, Milošević M, Simić V, Fallon BC, et al. An insight into perfusion anisotropy within solid murine lung cancer tumors. Pharmaceutics. 2024;16(8):1009. doi: 10.3390/pharmaceutics16081009.

Milosevic M. CAD Solid and Field: software for biomedical engineering research. 2020. Available from: https://github.com/miljanmilos/CAD-Solid-Field.

Milosevic M, Simic V, Milicevic B, Koay EJ, Ferrari M, Ziemys A, et al. Correction function for accuracy improvement of the composite smeared finite element for diffusive transport in biological tissue systems. Comput Methods Appl Mech Eng. 2018; [Epub ahead of print]. doi: 10.1016/j.cma.2018.1004.1012.

Sevick EM, Jain RK. Geometric resistance to blood flow in solid tumors perfused ex vivo: effects of tumor size and perfusion pressure. Cancer Res. 1989;49:3506-12.

Smith NP, Pullan AJ, Hunter PJ. An anatomically based model of transient coronary blood flow in the heart. SIAM J Appl Math. 2002;62:990-1018.